ENGINEERING RESEARCH JOURNAL (ERJ)
Vol. 2, No. 51 April. 2022, pp.32-54
Journal Homepage: erj.bu.edu.eg

Experimental Study of 3D Confined Masonry Building under Cyclic Loading

Mohamed O.R. El-Hariri[a], Amr A.Gamal[a], Mosaad El-Diasity[b], Sayed Salah .H[c]

[a]Professor, Faculty of Engineering at Shoubra, Benha University.

[b]Assistant Professor, Faculty of Engineering at Shoubra, Benha University.

[c]Assistant Lecturer, Faculty of Engineering at Shoubra, Benha University.

Abstract. Since the dawn of human civilization, masonry has been used to construct all types of buildings, bridges, roadways and other engineering works. Confined masonry (CM) is considered one of the popular forms of low-cost and low-rise construction throughout the world. Confined masonry consists of non-reinforced masonry walls surrounded by concrete tie-columns, in the vertical direction, and tie-beams, in the horizontal direction. In some countries confined masonry walls may include joint reinforcement. The behavior of constrained masonry structures under cyclic lateral loads was investigated in this experimental research. The two-story half-scale model was made using local materials and standards in consideration. With increasing displacement, lateral cyclic loads were applied to the model. Crack pattern, failure mechanism, lateral capacity, energy dissipation, ductility, and overall structural performance were all evaluated. Out of plane walls provided additional restrictions for wall movements and increased structural performance, while masonry infill walls provided significant strength and ductility. The findings show that confined masonry structures constructed to the standard will withstand the design lateral loads successfully. The case study for the tested assembly was verified using finite element model verification using experimental results. The developed model is capable of accurately capturing the maximum load and its related deformation of the tested structure, according to the results of the finite element analysis. For fracture patterns and failure mechanisms, the suggested model agrees well with the results of laboratory tests.

KEYWORDS: Confined Masonry, experimental study, Seismic Behavior, Cyclic loading, Shear Failure, Structural behavior factor; Drift; Strength; Stiffness; Energy dissipation.

1. INTRODUCTION

Masonry systems come in a wide range of shapes and sizes, and they've been employed as a structural material for thousands of years. Some very old stone and brick masonry structures still remain, demonstrating that masonry can withstand loads and environmental influences. (E Abdulahad and E Mahmud et al. 2018[1]). The confined walls are distinguished because tie-columns and tie-beams are typically cast in place after masonry has been built, forcing the masonry and concrete elements to act as an integral unit when the wall is subjected to lateral loads. (J. Martin Leal-Graciano et al. 2020[2]).

Past earthquakes have revealed satisfactory performance of confined masonry as compared to unreinforced masonry buildings. For instance, during Chilean earthquake, 16% of the CM houses were partially collapsed as compared to complete collapse of 57% of unreinforced masonry houses (Ajay Chourasia et al.2020 [3]). Confined masonry is a structural system consisting of unreinforced masonry panels surrounded by horizontal and vertical “confining” members called bond beams and tie columns. Confined masonry building technology is similar to both reinforced masonry and reinforced concrete frame construction with infill walls.

In reinforcement masonry, Vertical and horizontal reinforcing bars are provided to enhance the strength and ductility (deformability) of masonry walls. In confined masonry, the reinforcement is concentrated in vertical and horizontal RC confining elements whereas the masonry walls are usually free of reinforcement.

In confined masonry construction, masonry walls are constructed first, one story at a time, followed by the cast in-place RC tie-columns. Finally, RC tie-beams are constructed on top of the walls, simultaneously with the floor/roof slab construction. In RC frame construction infilled with masonry panels, the frame is constructed first, followed by masonry construction.

Confined masonry buildings have demonstrated satisfactory performance in past earthquakes. Latin America is certainly the first region of the world where CM construction is used widely and was successfully tested in several earthquakes associated with the regions of high seismic risk (Mosaad El-Diasity, 2015[4]).

Seismic behavior of CM wall can be showed by composite (monolithic) action of a masonry wall and adjacent RC confining elements. This composite action was found due to the toothing between the walls and the tie-columns. In absence of toothing, composite action can be made by means of reinforcement (horizontal dowels) (Jhair Yacila et al, 2019[5]). Studying a two-bay CM specimen that was subjected to reversed cyclic lateral loading simulating earthquake effects (Perez G., et al, 2009 [6], Choayb Belghiat et al., 2021 [7]). The specimen showing a typical damage pattern in the shape of diagonal shear cracks. The failure took place in the form of a signal diagonal crack which was propagated through the walls and through the tie-columns.

Confinement, in fact, alters the failure mode of URM walls and slows down the rate at which stiffness would decay, therefore improving the post-cracking seismic performance of CM walls. Peak point of the recorded response which defines the maximum load state is usually sustained at the extension of cracks into tie-columns ends.

Earthquake-induced lateral forces in multi-story CM building, peak at ground floor level and may cause significant shear cracking. Under severe earthquake ground shaking, the collapse of a CM building can take place at the first story level (Svetlana Brzev et al 2015 [8]).

Shear capacity of a CM wall panel can be determined as the sum of contributions of the masonry wall and the adjacent RC tie-columns. Note that the shear capacity of tie-columns can be reached only after the masonry has been severely cracked and its shear capacity has significantly decreased (Roberto M., et al. 2011[9]).

In the last two decades, several seismic retrofitting techniques for masonry walls have been developed and practiced such as using GFRP sheets or laminates, CFRP strips, cable system, and wire mesh mats. It was observed that FRP upgrading improve the wall lateral resistance by a factor ranging from 1.3 to 2.9 and the X shape upgrading configuration had the maximum drift of all specimens(Mosaad El-Diasity et al, 2015[4]).

2. EXPERIMENTAL PROGRAM

In this study, a CM building was constructed to achieve the objectives of experimental program. The experimental program intended to assess experimentally the lateral performance of un-retrofitted 3D CM buildings with various configurations under cyclic loading. Two phases were implemented in this experimental program. It was also intended to develop and validate FE numerical model to simulate the response of the CM buildings to confirm the model capacity to predict the behavior of untested configurations. Another aim was to evaluate the seismic performance parameters of un-retrofitted CM building such as ductility factor, energy absorption, stiffness degradation, and damping.

2.1 Material properties

A base concrete mixture made with ordinary Portland cement and water-to-cement ratio (w/c) of 0.45 at a nominal compressive strength of 25MPa was used to prepare all concrete elements. Mixture design was performed at the Reinforced Concrete Laboratory at the Faculty of Engineering at Shoubra. Compressive strength testing of cubes was performed according to The Egyptian Guide for Lab Testing of Concrete Materials (ECCS203-2018[10]). The average compressive strength (fcu) for each concrete element is presented in Table 1. Locally produced steel rebars of grades were used in this study. For bar sizes of 6mm and 8mm, mild

steel smooth rebars of grade B240D-Rthat have minimum yield strength (Fy) of 240 MPa and ultimate tensile strength (Fu) of 300 MPa were used For bar diameters of 10mm and 12mm, high tensile steel deformed rebars of grade B400DWR with a proof strength of 400MPa and ultimate tensile strength of 500 MPa were applied. Cement mortar specimens were prepared with cement: sand of 1:3 with the w/c was set at 0.5. Compressive strength testing of specimens was performed according to The Egyptian Guide for Lab Testing of Concrete Materials (ECCS203-2018 [10]).The average compressive strength (fcu) was 20.3 MPa. The mortar was used to bind the clay masonry units together in the walls**.** Local full cored clay block units having dimensions of 200 x 95 x 60 mm, (length x width x height) were used in the research, which were provided by a local manufacturer located at Helwan City, Cairo, following handmade procedures in the production. The average nominal compressive strength of the masonry units was 7.0MPa

2.2 Specimen dimensions

A sample two storey CM building was made at a scale of 0.50, with plan dimensions of 1.50 x 1.50 m and total height of 2.60 m. The building was constructed on a raft foundation (thickness of 0.30 m) made with the base concrete mixture mentioned in Section 2.1. Raft edges were extended for 0.35 m beyond the boundaries of the building (i.e. raft plan dimensions were 2.20 x 2.20 m) to allow for safe resistance against overturning during the lateral load subjection process. Raft was reinforced with top and bottom layers using 12 mm diameter longitudinal bars at 200 mm c/c.

Each storey was built using single Wythe brick wall (a vertical section of bricks with a thickness of one unit 95 mm in this study. The brick units were laid according to running bond method (a type of masonry bond in which each brick is placed as a stretcher and overlaps the bricks in adjoining courses) using 10 mm mortar defined at section 2.1.

The wall systems were confined with two reinforced concrete tie-columns at edges and one tie-beam on top, supporting 150 mm thick reinforced concrete slab. The tie-columns were of size 150 x 150 mm and reinforced with 4T10 mm longitudinal bars and 6 mm diameter ties at 200 mm c/c. Tie-beams (150 x 150 mm) were located at slab level with 4T10 mm longitudinal bars and 6 mm diameter ties at 200 mm c/c. Figure 1 shows a typical plan and cross-section, showing RFT details for the building.

Each story had two solid walls, one wall perforated with a window opening of size 0.34 x 0.34 m, and one perforated wall with a door opening of size 0.36 x 0.64 m, as shown in Figure 2

2.3 Specimen Fabrication

Construction of the specimen started with casting of RC raft to safely support each building. Steel RFT cage was initially formed with top and bottom layers of T12 @ 200 mm and fixed in position, followed by assembling a timber formwork surrounding the reinforcement steel cage. Three rows (spacing 0.80 m) of two strong pre-tensile bolts (Ø50mm) [located 1.6 m apart] were fixed at the form. Next, concrete with compressive strength of 25 MPa was poured manually into the formwork with concurrent consolidation using electric vibration.

An experienced mason built all masonry walls using the running bond pattern with 10 mm mortar bedding. Half bricks were deliberately left in alternate courses to create a toothed interlocking with tie-columns. Before setting up the formwork for tie-columns, multiple electrical steel strain gauges were glued on the longitudinal reinforcement. Formwork was then constructed for the tie-columns to maintain a size of 150x150mm with a toothed interlocking with masonry wall and 15 mm clear concrete cover. Tie-columns were reinforced with 4T10 mm longitudinal bars and 6 mm diameter ties at 200 mm c/c. Next, formwork for the top slab and tie-beams was installed, followed by casting of concrete to a thickness of 150 mm Concrete was then poured in the formwork and consolidated. Concrete was, then, cured after removal of formwork until the time of testing. Second floor was built according to the same procedure as the first storey. Work started with laying out masonry blocks to the required height. Afterwards, strain gauges were installed and tie-columns were casted followed by the tie-beams and top slab. Figure 3 shows a view during construction of the specimen. The specimen was painted with white pigment to allow for easy monitoring of cracking during the loading process.

Table 1. Average compressive strength results of different RC elements.

	Footings	Tie-columns first floor	Slab and tie beams first floor	Tie-columns second floor	Slab and tie beams second floor
fcu (MPa)	29.6	27.4	27.3	26.5	26.8

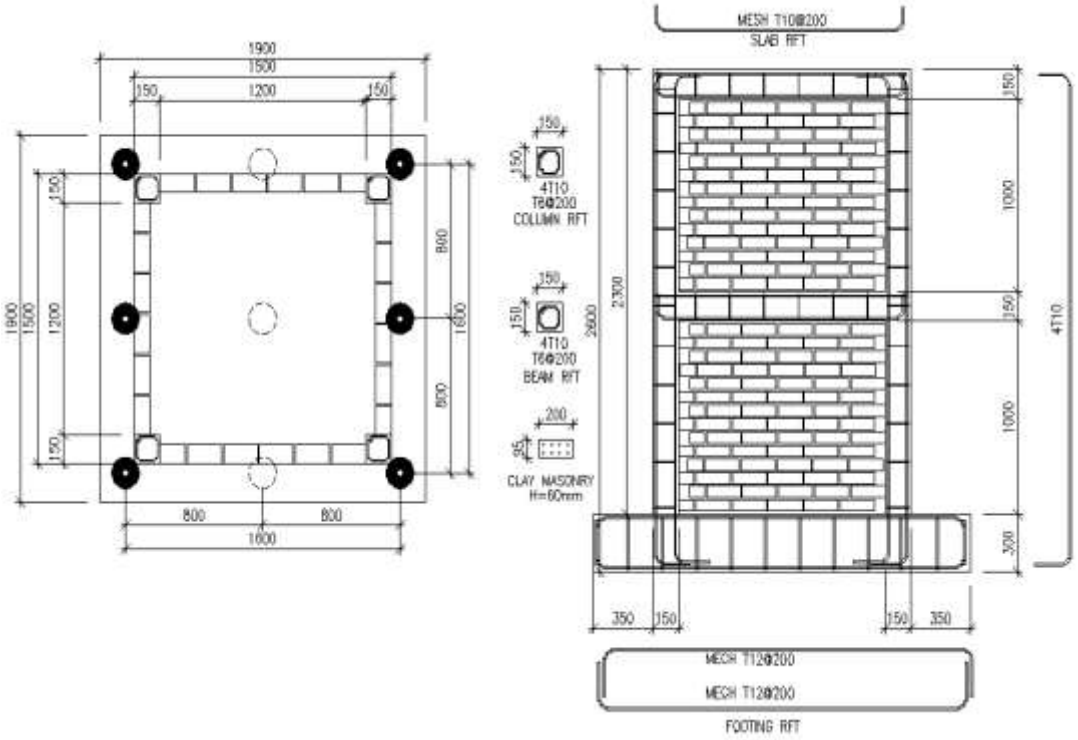

Figure. 1. Plan (left) and cross-section (right) of the CM building.

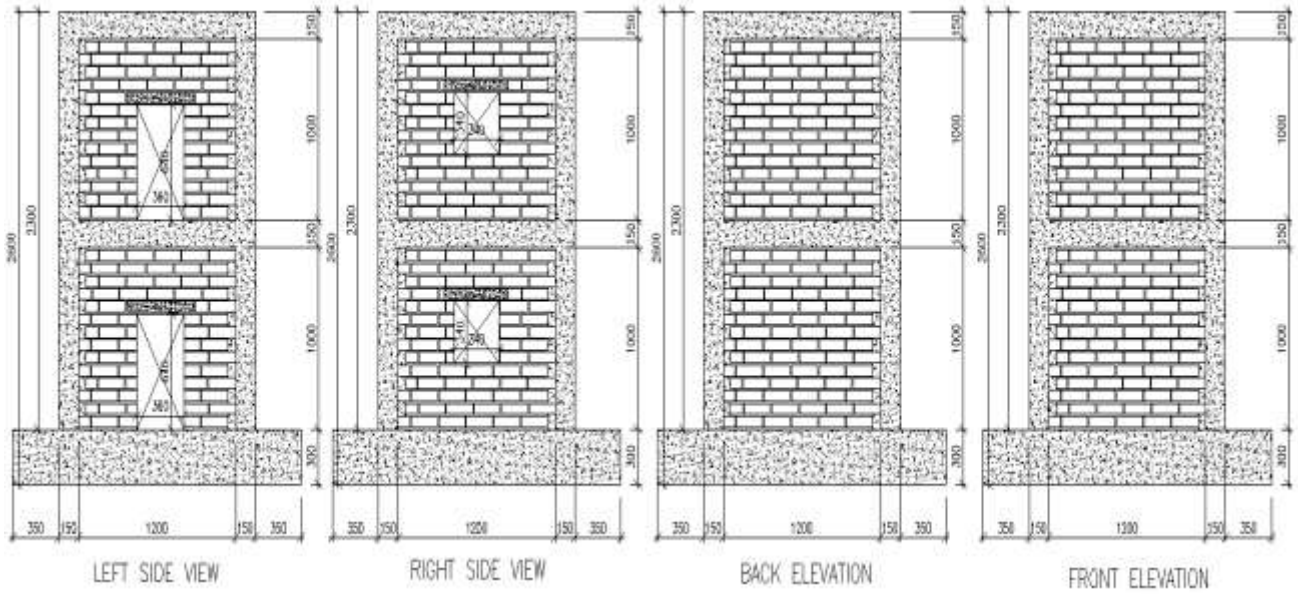

Fig. 2. Geometrical detail of typical (a), (b) solid walls, (c) wall perforated with window opening, and (d) perforated wall with door opening.

Fig.3. Construction process of specimen.

2.4 Testing Procedure

As mentioned, raft of all CM buildings was fixed to the reaction floor by sixØ50mmpre-tensile bolts (Figure 4) to prevent overturning and sliding of raft during the loading process.

The CM Building was subjected to a cyclic incremental lateral load until failure. Loading was applied using a 900 KN hydraulic actuator fixed at the roof level as shown in Figure 5, noting that a steel beam was added in between the jack plate and the finished surface of specimen to permit uniform loading at the roof level without localized fracture of building. The actuator works in two ways to permit reversed displacement-controlled loading. The horizontal hydraulic jack was connected to oil hydraulic pumps shown in Figure 6. The horizontal force was imposed to the building via control displacement at a rate of 60 µm/s; full displacement protocol was programmed for each amplitude increment with the purpose of strength and degradation assessment. The proposed displacement protocol (Figure 7) was designed to begin with small displacement increments to observe the building elastic behavior until the first crack occurs, followed by an incremental displacement increase during the plastic stage to monitor the building ductility and energy absorption until collapse. The preceding procedure was comparable to many sources, including (Tomazevic and Klemenc, 1997[11]). At the completion of each loading cycle, the displacement

was held constant for 2 minutes using a computer data acquisition system (Figure 8) to provide enough time for observing, identifying and measuring of visible cracks. The sample was oriented in such a way that loading was imposed perpendicular to the side of specimens with door perforations, as shown in (Figure 9). CM specimen was equipped with multiple electrical linear variable distance transducers (LVDTs) at key locations to measure displacements/strains of concrete and steel bars during loading. Six LVDTs were used with an accuracy of 0.01 mm and were coded LVDT-1 up to LVDT-6. Distance transducers were mounted on the two sides parallel to load direction; which were the two solid faces in locations as shown in Figure 10. LVDT-1 and LVDT-2 monitor the lateral displacement at the roof level point of the specimen, which represents the location of maximum expected lateral drift during loading. LVDT-3 senses any sliding of raft occurring during testing. The relative displacement between upper value measured by LVDT-1 or LVDT-2and the sliding amount determined by LVDT-3 is considered the actual lateral displacement acting at the top of building, caused by the horizontal jack according to the cyclic displacement protocol adopted for testing. The purpose of LDVT-4was to monitor any relative displacement occurring between the bottom point of masonry wall in first storey and the raft, which may occur if sliding and/or rocking failure modes were to control the failure of specimen. LVDTs 5 and 6 measured the diagonal crack width, occurring in the masonry panel for both push and pull directions. In addition, the described LVDTs aimed at monitoring the time history of master points of building to assist with continuous update of the specimen's geometry during the test.

Strain in the longitudinal reinforcement and lateral ties in tie-columns was monitored using eight electrical strain gauges (10 mm gauge length and 120 Ohm resistance); four gauges were mounted above raft while others were located slightly above slab of first storey with coding starts with SG-1 to SG-8. The strain gaugesSG-1, SG-3, SG-5, and SG-7 were used to determine the strain in longitudinal reinforcement of tie-columns while SG-2, SG-4, SG-6, and SG-8 monitored the strain at the first stirrup of tie-columns above raft [SG-2 and SG-4] and above slab of first storey [SG-6 and SG-8], respectively.

All LDVTs and strain gauges were linked to a data collection system operated by a computer. Throughout the duration of testing, displacement, crack width, loading values, and strains were constantly monitored and recorded until the CM building collapsed. Also, the crack patterns were continuously monitored and marked on the walls with the corresponding displacement level typed next to it.

2.5 Experimental results and discussion.

This section describes the developments in the condition of specimen at various stages of loadings; noting that only key points that show significant variation in damage was discussed.

Damage state1 (DS1): In the push direction, the first visible crack appeared at a lateral displacement of 4.00 mm and corresponding lateral load of -70KN. The crack initiated at the bottom corner of upper floor in the front and back elevation (solid faces in this case) and propagated upwards until reaching three-quarters of the floor clear height. The crack started diagonally and then had a vertical orientation parallel the closest column at an average distance of 250 mm, suggesting the. Similarly, reversing the direction of loading (pull direction) caused the first crack to occur at lateral drift of 4.25 mm and corresponding lateral load of +80KN. However, the crack shape was diagonal starting from the bottom corner (opposite to the push direction) all the way up to the upper midpoint of walls, implying the shear failure behavior of walls. It should be noted that no signs of cracking were noticed for the two sides of specimen with perforations. In addition, for this loading range, no cracks were developed within the bottom storey since the upper floor was directly exposed to loading and experienced the maximum drift. Thus, most of the energy was absorbed by the elements of upper floor and accordingly, the damage was manifested in the form of the vertical/diagonal cracking. Figure 11 shows the final condition of specimen at the end of this loading stage.

Damage state3 (DS3): During this stage of loading, the imposed lateral displacement was -8 mm and +4.5 mm in the push and pull directions, with a corresponding lateral loading of -110 KN and +100 KN, respectively. Pushing the specimens resulted in the development of a diagonal shear crack at the bottom corners of both floors (upper and bottom) reaching the opposite upper corners. In the pull direction, a diagonal crack initiated at the bottom corner of upper floor and propagated upwards up to the mid-point of tie-beam, with no noticeable cracks developed in the bottom floor. Generally,

the crack widths were slightly increased in this loading stage, as shown in Figure 12. Also, both sides perpendicular to the direction of loading remained intact without any signs of damage.

Damage state6 (DS6): At this stage, the imposed drift was 12 mm for both the push and pull directions with a corresponding lateral loading of 160 KN. The condition of the specimen at this stage of loading shows increased intensity of cracking in the upper floor. Horizontal cracks were developed at the bottom of tie-beam, as shown in Figure 13. In addition, the output cracks of previous stages propagated until the top corner of slab; also, widths of cracks were increased. For the bottom floor, a diagonal crack was developed in the pull direction between two opposite corner points, indicating the shear failure behavior of specimen. Also, a horizontal crack was noticed 250 mm above the top surface of foundation, which may refer to a flaw in the masonry units at this location of specimen. Regarding the sides with openings, few horizontal cracks were found around the locations of openings supposing the participation of those sides in the dissipation of energy after the sufficient cracking of solid walls; noting that, cracks were mainly horizontal due to tensile stresses developed at these points (i.e mortar beds due to the inability of masonry/mortar to support tensile stresses beyond their capacity) during the push and pull loadings.

Damage state10 (DS10): Figure 14 shows the final condition of specimen at failure. The specimen could not sustain extra levels of loading. The specimen start to disintegrate and chunks of masonry fell from the upper storey. During this stage, the imposed lateral displacement was -26 mm for both the push and pull directions, with a corresponding lateral loading of -182 KN and +221 KN, respectively. The intensity of cracks significantly increased at this stage within the solid walls (main load resistant frames), especially for the upper floor due to its proximity to load. The final shape of cracks resembled a cross-mark for both top and bottoms floors, confirming the shear failure behavior of the specimen. No cracks were observed within the columns and foundation of specimen; nearly all cracks were formed within the masonry walls between the reinforced concrete elements, endorsing the benefits of infilled-masonry structures. Table 2 shows the damage stage of model specimen from DS1 to DS 10 until the specimen reached to failure.

The relative Hysteresis loops and Envelope curve for the 3D model assembly sample are shown in Figure 15 as the solid lines indicate to load-displacement relationship for each cycle, and the bold dashed line indicates to envelope curve that connect the end values of cycles. The figure indicates that initial stiffness of specimen was high so the initial relative loads for small displacements were great. After the first crack in pushing side appeared, the stiffness was reduced with increasing top displacement. The maximum lateral load was +182 KN relative to +22 mm lateral top displacement and -221KN relative to -20mm top displacement.

The relative cumulative Energy Dissipation curve for the 3D model assembly sample is shown in Figure 16. The Total cumulative dissipated energy at end of result was 7.17KN.m at ultimate displacement equals +22mm.

The corresponding Hysteresis Damping percentages curve for the 3d model assembly sample is shown in Figure 17. The minimum, average, and maximum damping percentage values are 3.59%, 4.51%, and 5.61% respectively. The obtained values are matching the range stated for specimens with dimensions, loading, materials nearly similar to the tested assemblies by (Angelo M. and Enrique C. 2004 [12]). The relative Secant Stiffness curve for the sample is shown in Figure 18. The initial stiffness was tend to be 43.5 KN/mm but after first crack has been appeared, the specimen stiffness reduced to be 32 KN/mm (about 27% of initial stiffness). With increasing the lateral top displacement and the resisting lateral load, the stiffness reduced according to cracking propagation. The stiffness of specimen at maximum capacity (at lateral displacement +22 mm) equals 11 KN/mm (about 13% of initial stiffness. Similar values of reduction in specimen stiffness were recorded by (Angelo M. and Enrique C. 2004 [12]).

Fig. 4. Fixing the raft to the reaction floor.

Fig 5. Hydraulic jack fixed at roof level.

Fig. 6. Oil Hydraulic pumps used in testing.

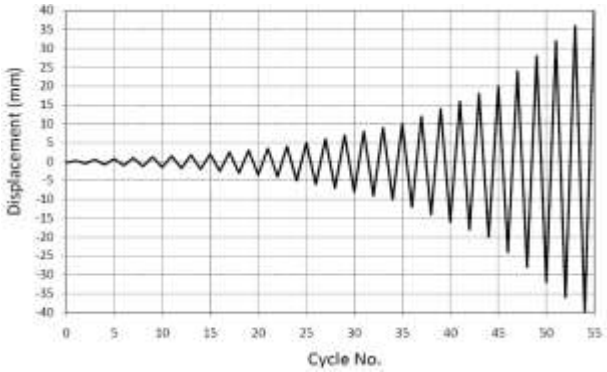

Fig. 7. Cyclic displacement protocol

Fig. 8. Computer controlled data acquisition system.

Fig. 9. Orientation of sample (Relative to loading direction).

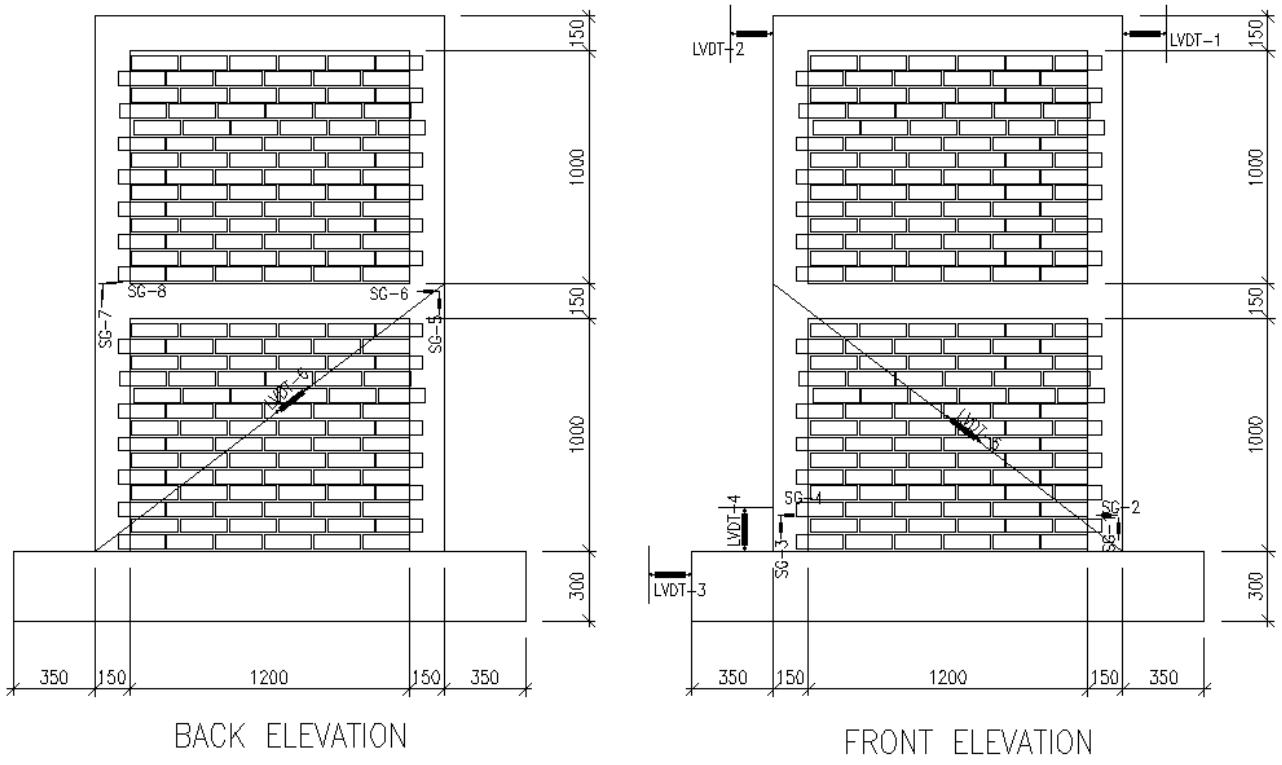

Fig 10. Locations of LVDTs in the specimen

Fig.11. DS1 first cracks at upper floor

Fig. 12. DS3 Diagonal shear crack

Fig. 13. DS6 Propagated Diagonal Shear cracks

Fig. 14 DS10 Diagonal shear crack at bottom

The relative strain of longitudinal reinforcement at left column in front elevation for the specimen is shown in Figure 19.a. The steel was yielded (ξ=0.0025) at lateral load equals 220 KN which is nearly the cracking load of specimen and the strain of first lower stirrup in left column is shown in Figure 19.b. The ultimate strain at failure reached 0.0009 relative to lateral load equal 220 KN. The relative strain of longitudinal reinforcement at right column in front elevation for the sample is shown in Figure 19.c. The steel was yielded (ξ=0.00009) at lateral load equals 175 KN. The relative strain of longitudinal reinforcement at right column in back elevation for the sample is shown in Figure 19.d. The steel was yielded (ξ=0.002) at lateral load equals100KN. Figures 20.a, 20.b, 20.c and 20.d show as examples the lateral deformation of the Specimen. These deformations were obtained with the LVDT used to measure the relative horizontal and vertical displacements between the 3d specimen and the foundation and walls at different heights. Figures 20.a, 20.b, 20.c and 20.d show as examples the lateral deformation of the Specimen. These deformations were obtained with the LVDT used to measure the relative horizontal and vertical displacements between the 3d specimen and the foundation and walls at different heights. Figure 20.a shows displacement of diagonal LVDT in front elevation of the specimen to measure the width of cracks happened in the front elevation, where the maximum crack width 23.5mm at load 175 KN. Figure 20.b shows displacement of horizontal LVDT in front left of footing for the specimen to measure the maximum movement of footing during testing of the specimen, where the maximum displacement 0.75mm at load 175 KN. This value of displacement is too small to affect in the test. Figure 20.c shows displacement of vertical LVDT in front left of footing for the specimen to measure the overturning movement of footing during testing of specimen the specimen, where the maximum displacement 1.3mm at load 220 KN. This value of displacement is, also, too small to effect in the test. Figure 20.d shows displacement of vertical LVDT in right left of footing for the specimen to measure the overturning movement of footing during testing of specimen the specimen, where the maximum displacement 1.3mm at load 160 KN. This value of displacement is, as well, too small to effect in the test.

Table 2. Damage States Summary of Tested model Specimen.

Damage state	Push		Pull		Cracks
	Load (KN)	Drift (mm)	Load (KN)	Drift (mm)	
DS1	-70	-4.0	-	-	The appearance of an upper first crack under the beam of the second floor
	-	-	+80	+4.25	
DS2	-65	-3.0	-	-	-
	-	-	+85	+3.5	
DS3	-110	-8.0	-	-	Diagonal shear crack
	-	-	+100	+4.5	
DS4	-110	-8	-	-	The appearance of an lower crack under the beam of the second floor
	-	-	+122	+6	
DS5	-140	-10	-	-	-
	-	-	+140	+10	
DS6	-160	-12	-	-	-
	-	-	+160	+12	
DS7	-165	-14	-	-	-
	-	-	+180	+16	
DS8	-180	-20	-	-	Diagonal crack 6mm at top
	-	-	+200	+20	Diagonal crack 3mm at bottom
DS9	-181	-24	-	-	diagonal cracks crack width 9 mm
	-	-	+210	+22	
Ds10	-182	-26	-	-	Failure Shear diagonal at top level
	-	-	+221	+26	

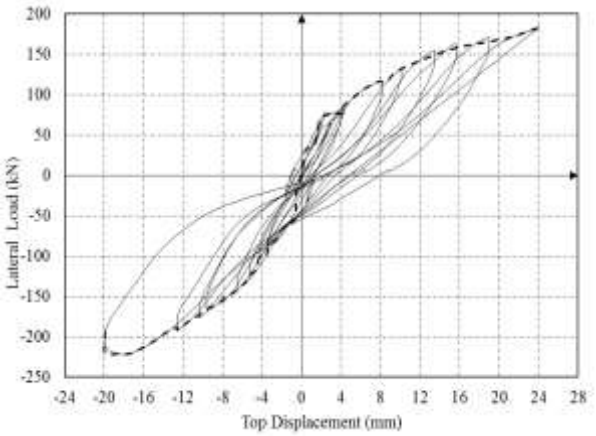

Fig. 15. Hysteresis loops and Envelope curve

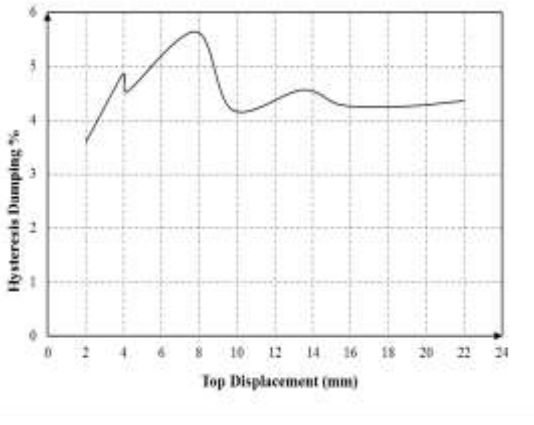

Fig.17.Hysteresis damping percentages curve

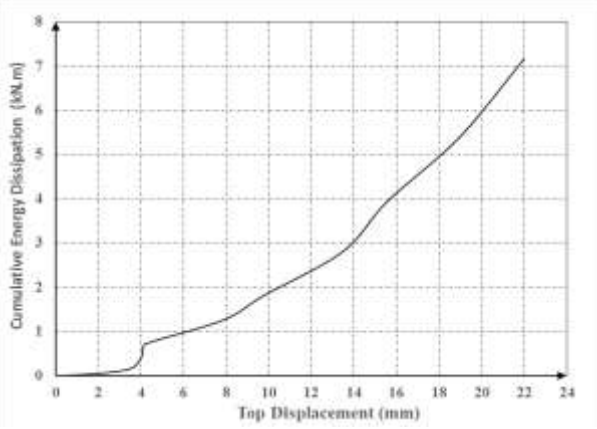

Fig .16 .Cumulative Energy Dissipation curve

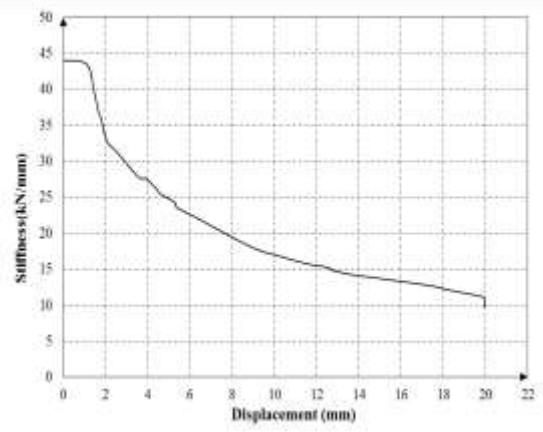

Fig. 18. Stiffness Degradation curve

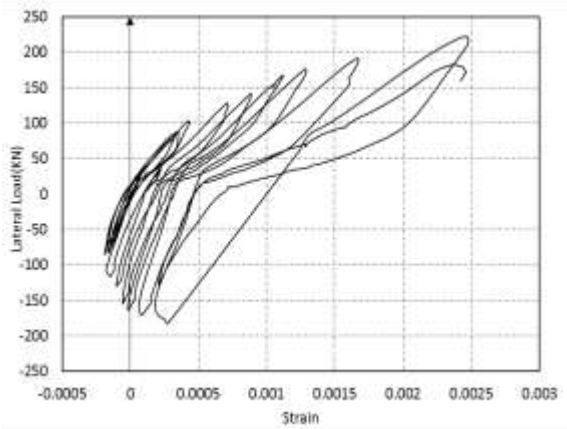

Fig. 19. A –Strain in longitudinal reinforcement of left column in front elevation

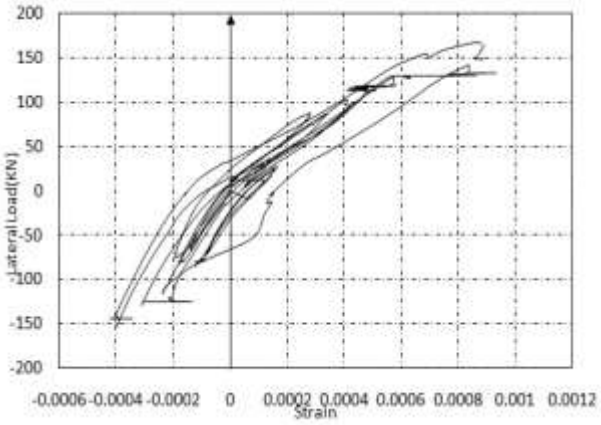

Fig. 19. B Strain in first lower stirrup in left column

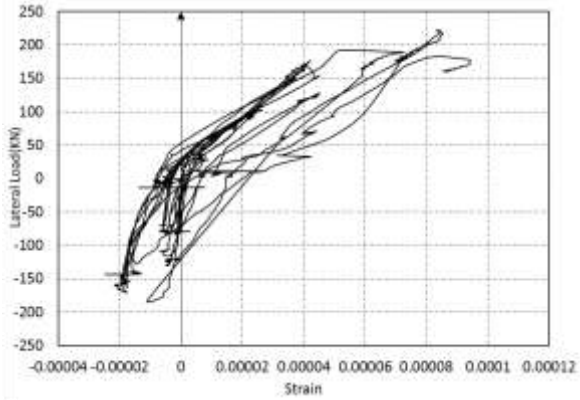

Fig.19.C – Strain in longitudinal reinforcement of column right column in back elevation

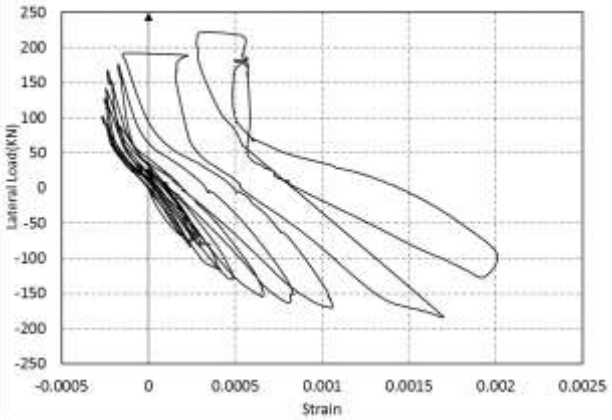

Fig. 19. D Strain in longitudinal reinforcement of right column in front elevation

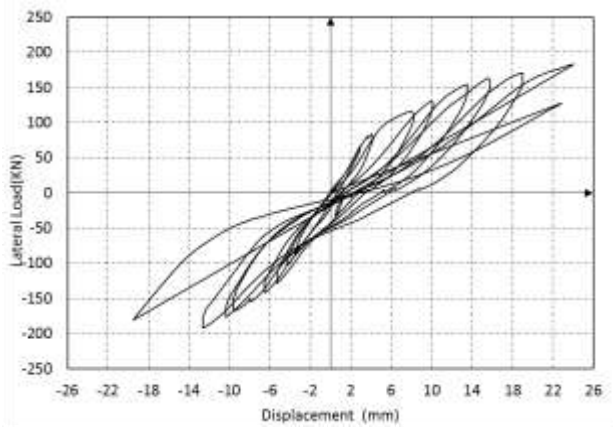

Fig .20.A. Displacement of diagonal LVDT in front elevation of the specimen

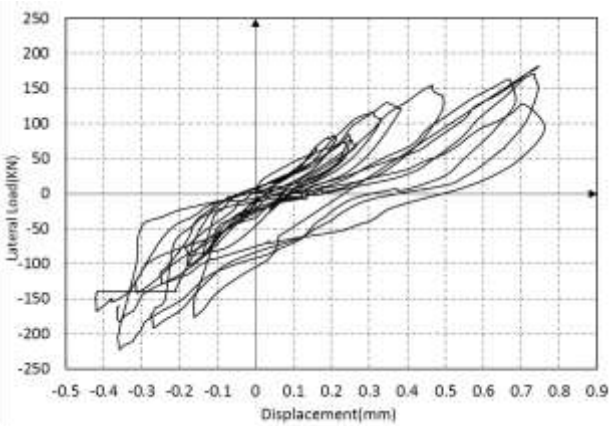

Fig. 20. B. displacement of horizontal LVDT in front left of footing for the specimen

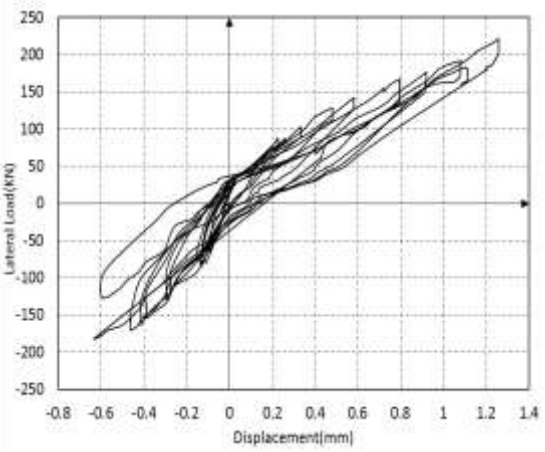

Fig. 20. C. Displacement of vertical LVDT in front left of footing for the specimen

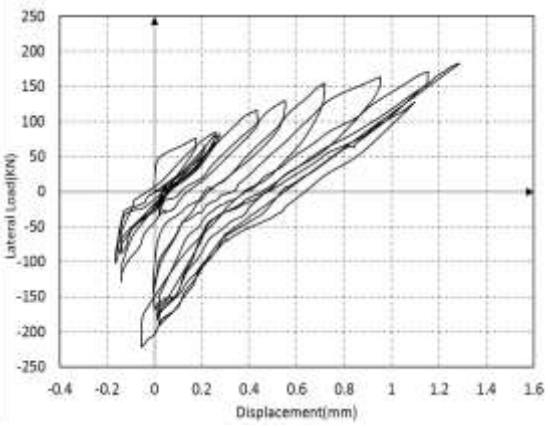

Fig. 20. D. displacement vertical LVDT in right left of footing for specimen

3. EXPERIMENTAL PROGRAM

It was aimed to create 3D finite element model for the tested 3d structure assembly that are capable of capturing the essential response aspects of failure mode shapes and crack patterns for specimen and comparing them to experimental results and previous references to verify them.

3.1 Theoretical Description of Elements

A computer package called "ANSYS® [13]" was used to do the non-linear finite element analysis. To model the concrete and bricks (SOLID65), an 8-node solid element with three translational and additional rotational degrees of freedom at each node was used, whilst the steel rebar's were modelled using a 2-node bar element (LINK8).

Within each element, SOLID65 allows for the presence of up to four different materials: one matrix material (e.g. concrete) and up to three independent reinforcing materials. In addition to combining plastic and creep behavior, the concrete material is capable of directed integration point cracking and crushing. The reinforcement has only uniaxial stiffness and is considered to be spread throughout the element (it also comprises creep and plasticity). Angles set by the user are used to achieve directional alignment.

Link 8 is an engineering spar that can be utilized in a variety of applications. The element can be thought of as a truss element, a cable element, a link element, a spring element, and so on, depending on the application. The three-dimensional spar element is a tension-compression uniaxial element with three degrees of freedom at each node: nodal x, y, and z translations. No bending of the element is taken into account, as it is in a pin-jointed structure. Plasticity, creep, swelling, stress stiffening, and significant deflection capabilities are all part of the package.

SHELL43 excels at simulating linear, distorted, somewhat thick shell structures. At each node, the element has six degrees of freedom: translations in the x, y, and z directions, as well as rotations around the x, y, and z axes. In both in-plane directions, the deformation shapes are linear. It employs a mixed interpolation of tensorial components for out-of-plane motion. Plasticity, creep, stress stiffening, large deflection, and huge strain capacities are all features of this element.

3.2 Material Modeling

Material idealization and material characteristics are extremely important in nonlinear analysis. The capacity to forecast the failure of brittle materials is a feature of the concrete material model assigned to the Solid65 element used throughout this work. The failure modes of cracking and crushing are also taken into account. The criterion for concrete failure owing to a multi axial stress state is as follows:

$$\frac{F}{f_c} - S \geq 0 \qquad \text{(Eq. 1)}$$

where:

F = a function of the principal stress state;σxp, σyp, σzp;

fc= uniaxial crushing strength;

S = failure surface expressed in terms of principal stresses and the strength;

Parameters ft, fc, fcb, f1 and f2;

ft = ultimate uniaxial tensile strength;

fc = ultimate uniaxial compressive strength;

fcb= ultimate biaxial compressive strength;

f1 = ultimate compressive strength for a state of biaxial compression superimposed

on hydrostatic stress state;

f2 = ultimate compressive strength for a state of uniaxial compression

Superimposed on hydrostatic stress state.

Both the function F and the failure surface S are expressed in terms of principal stresses denoted as σ_1, σ_2 and σ_3 where $\sigma_1 = max(\sigma_{xp}, \sigma_{yp}, \sigma_{zp})$, $\sigma_3 = min(\sigma_{xp}, \sigma_{yp}, \sigma_{zp})$,and $\sigma_1 \geq \sigma_2 \geq \sigma_3$.

The failure of concrete is categorized into four domains:

$0 \geq \sigma_1 \geq \sigma_2 \geq \sigma_3$ (compression-compression-compression)

$\sigma_1 \geq 0 \geq \sigma_2 \geq \sigma_3$ (tensile - compression - compression)

$\sigma_1 \geq \sigma_2 \geq 0 \geq \sigma_3$ (tensile - tensile - compression)

$\sigma_1 \geq \sigma_2 \geq \sigma_3 \geq 0$ (tensile - tensile - tensile)

Independent functions describe the function F and the failure surface S for each domain. F1, F2, F3, and F4 are the four functions that describe the general function F, while S1, S2, S3, and S4 are the four functions that describe S. Figure 21 depicts the failure surface as a 3-D failure surface in principal stress space. The relative magnitudes of the primary stresses are described by the angle of similarity. The 3-D failure surface for biaxial or nearly biaxial stress states is represented by the failure surface in primary stress space with nearly biaxial stress, as shown in Figure 22. If the most significant non-zero principal stresses are in the σxp and σyp directions, the three surfaces presented are for σzp slightly greater than zero, σzp equal to zero, and σzp slightly less than zero. Although the three surfaces, shown as projections on the σxp - σyp plane, are nearly equivalent and the 3-D failure surface is continuous, the mode of material failure is a function of the sign of σzp. For example, if σxp and σyp are both negative and σzp is slightly positive, cracking would be predicted in a direction perpendicular to the σzp direction. However, if σzp is zero or slightly negative, the material is assumed to crush.

Input strength parameter sft, fc, fcb, f1 and f2 are needed to define the failure surface as well as an ambient hydrostatic stress state. The ultimate uniaxial compressive strength fc, was taken 20 MPa based on the studied bar frame by Mehrabi et. al. (1996) and ft was taken as recommended by ACI specifications, (ft= 0.1 fc).The other parameters were taken as.

fcb= 1.2 fc, f1= 1.45 fc, and f2= 1.725 fc (Eq.2)

Shear transfer coefficients typically range from 0.0 to 1.0, with zero indicating a very smooth fracture (total loss of shear transfer) and 1.0 indicating a very rough crack (no loss of shear transfer). Both the open and closed cracks can benefit from this feature. The open crack shear transfer coefficient was 0.6, and the closed crack shear transfer coefficient was 0.8. The analysis took into account a stress relaxation after cracking value of 0.3. According to various trail experiments, these values provide better performance for the frame load-deflection curve.

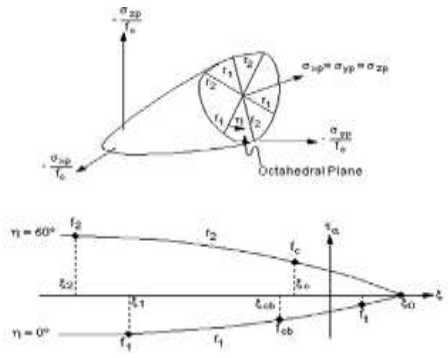

Fig.21. Failure Surface in Principal Stress Space

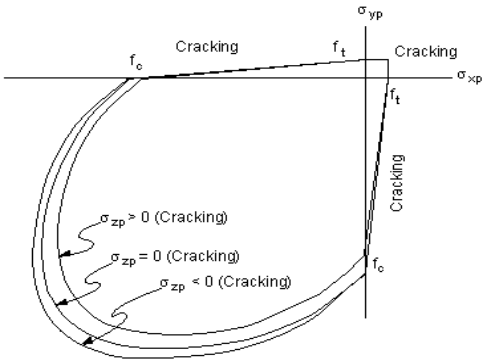

Fig. 22. Failure Surface in Principal Stress Space with Nearly Biaxial Stress.

In modeling of steel reinforcement, the stress-strain connection is represented by two straight lines, as provided by Taijum Wang [2001]. Figure 23 shows the average stress-strain curve of steel bars implanted in concrete

For $\varepsilon_s \le \varepsilon_n$

$$f_s = E_s \varepsilon_s$$

(Eq. 3)

and for $\varepsilon_s \ge \varepsilon_n$

$$f_s = f_y \left[(0.91 - 2B) + \left(0.02 + 0.25B \frac{\varepsilon_s}{\varepsilon_y} \right) \right]$$

(Eq. 4)

where fs and εs are the average stress and strain of steel bars, respectively; fy and εy are the yield stress and strain of steel bars, respectively; Es is the young's modulus of steel reinforcement; and $\varepsilon_n = \varepsilon_y (0.93 - 2B)$. The parameter B is given as $\left(f_{cr} / f_y \right)^{1.5} / \rho$, with ρ is the reinforcement ratio, and fcr is the cracking strength of concrete. The recommended value of fcris given as.

$$f_{cr} = 0.31 \sqrt{f_c'}$$ in MPa

(Eq. 5)

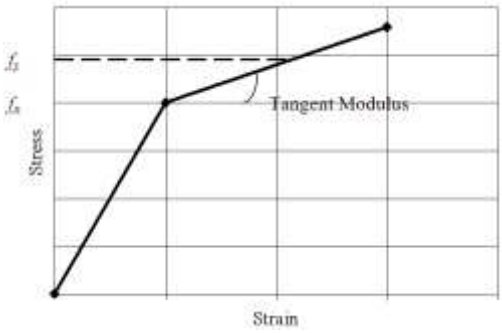

Fig .23. Modeling of Steel Using Bilinear Kinematic Hardening

The capacity to forecast the failure of brittle materials is a feature of the masonry material model assigned to the Solid65 element. The failure modes of cracking and crushing are both considered (Referring to the previously stated parameters). (Hemant, et al. 2007 [14]) recommended stress-strain curves for masonry prisms were scaled down with the same trend line to meet the properties of the employed bricks and mortar.

Eight masonry prisms were tested in order to evaluate the mechanical properties (masonry characteristic compressive strength f'm), these tests were performed to evaluate the stress-strain curve for masonry constructed from units available in the local Egyptian market. Although many curves can really be found in text books and other references (Hemant, et al. 2007 [14]), Figure 24 depicts the experimental, reference, and adopted curves, with the adopted curve able to anticipate the failure load and load displacement curve with acceptable accuracy.

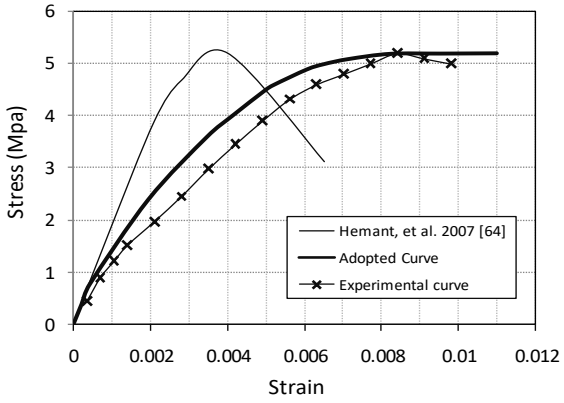

Fig. 24. Compressive stress-strain curves for masonry

Hemant B. Kaushik1; Durgesh C. Rai2; and Sudhir K. Jain, (2007), "Stress-Strain Characteristics of Clay Brick Masonry under Uniaxial Compression", Journal of Materials in Civil Engineering, Vol. 19, No. 9, ASCE, pp. 728-739.The predicted lateral load capacity and failure mode obtained from the model with cyclic loading was examined against the test experimental results.

3.3 Non-Linear Finite Element Verification

The Non-linear finite element verification model have three main goals, which are to illustrate the efficiency of the proposed model; verify element and material models; and validate the software program. The Boundary conditions for the models achieved to match the actual conditions in experimental test as the supporting of footing was achieved by lock the translation X, Y, Z at the same locations of the anchors which had been presented in the experimental program, and selected nodes on bottom edge of footing were locked against vertical and out of plan translation as shown in Figure 25

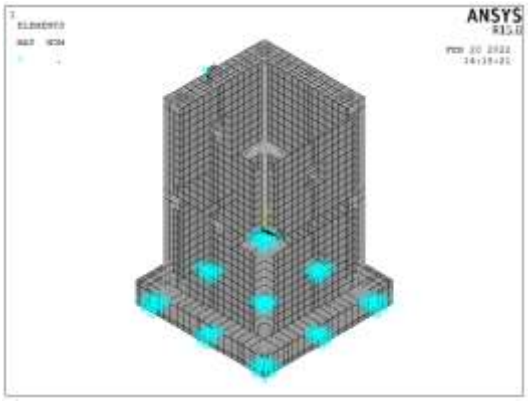

Fig. 25. Boundary conditions and location of horizontal load beam stup

Figures 26a to 26i show the cracking patterns obtained from finite element model at cracking load, at maximum load, and finally at ultimate or failure load which can be acceptable with good agreements with compared to cracking patterns of experimental test.

The shear stresses at ultimate load is shown in Figures 27i to 27l which clarify that shear stresses in masonry panel have average value of 0.8 Mpa at the diagonal compression strut which is nearly equals to the maximum derived shear stresses for tested wallets, where the calculated values for maximum shear stresses equal 0.77-0.81 MPa. Also the shear stresses at tie-columns reach ranges of 2.75-3.67 MPa which may be classified as accepted maximum shear stresses values for reinforced concrete with average compressive strength 26.0 - 27.5 Mpa as mentioned previously.

The mechanical strain at ultimate load is shown in Figures 27m to 27q where the strain in masonry ranging from 0.0075 to 0.058 which may be accepted by the suggested values derived and stated by (Hemant, et al. 2007 [14]) as the proposed ultimate strain equals 0.006.

The load- displacement envelope curves from the test and the finite element model are shown in Figures 28.a,b the maximum lateral loads of finite element model are +218 KN and -217 KN for pushing and pulling directions with compared to +182 KN and -221 KN obtained from experimental test with good agreement level to predict the maximum lateral capacity of specimen.

The corresponding lateral top displacements at maximum lateral loads from finite element model are +30mm and -28mm respectively for pushing and pulling directions. These values obtained from numerical analysis are nearly equal the corresponding experimental values which equal +24.0mm and -20.0mm, so good agreement can be achieved by finite element modeling to predict the corresponding deformations at maximum lateral load capacities.

The ultimate lateral loads of finite element model are equal +218 KN and -217 KN with compared to +182 KN and -203 KN as per experimental test which are slightly different. The corresponding lateral ultimate displacements at numerical model are +30.0mm and -28.0mm with compared to +24.0mm and -20.0 mm as per experimental result, so the ultimate displacements in finite element model were larger than its in experimental works which indicated that the plastic strains and softening after major cracks occurs are greater in experimental case than the numerical approach specially for masonry panel. Results from the finite element model of showed that the developed model is capable, with sufficient degree of accuracy, to capture the maximum load and its corresponding deformation of the tested wall but the ultimate displacements in model was larger than it is in experimental works. The relative Secant Stiffness

curve is shown in Figure 28c, the initial stiffness of FEM model about 95% of its value of experimental model. The relative cumulative Energy Dissipation curve is shown in Figure 28d. The Total cumulative dissipated energy at end of result were 7.2KN.m and 4.0KN.m at ultimate displacement equals +22.0mm.

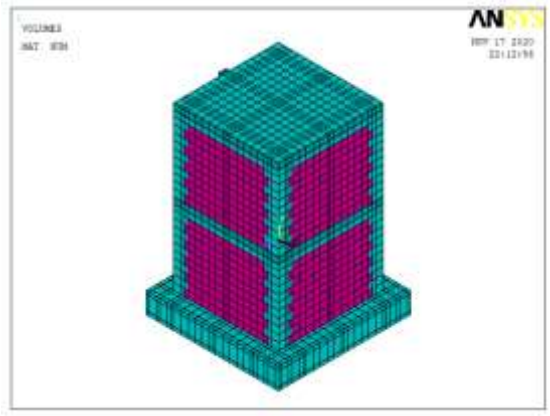

Fig. 26. A. Meshing of finite element for specimen

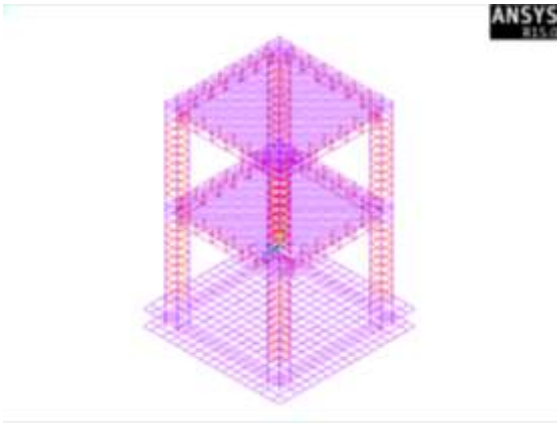

Fig. 26. B. Reinforcement of specimens

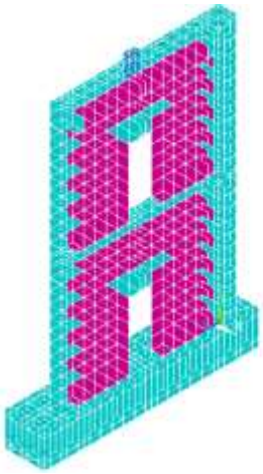

Fig. 26.C. Typical meshing (Doors opening).

Fig 26.D. Typical meshing (Windows Opening)

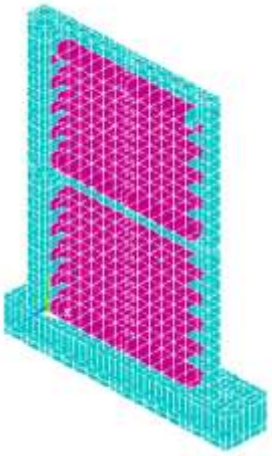

Fig. 26. E. Typical finite element meshing (solid walls).

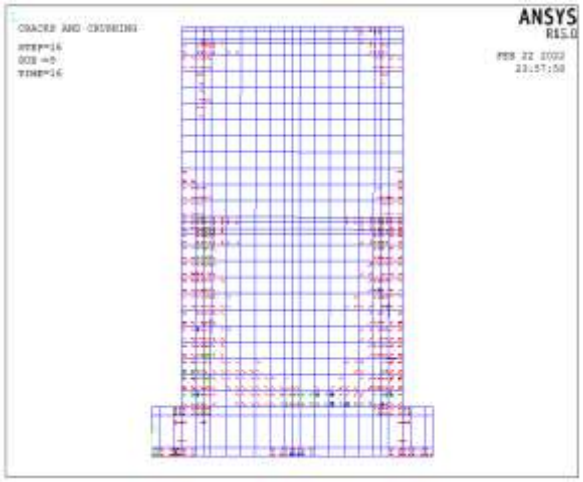

Fig. 27. A. Cracking pattern at cracking load (at frisk crack) for solid face

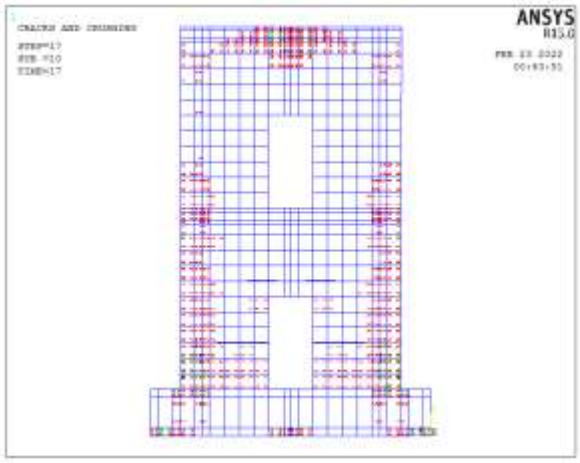

Fig.27.B. Cracking pattern at cracking load (at frisk crack) for face with doors

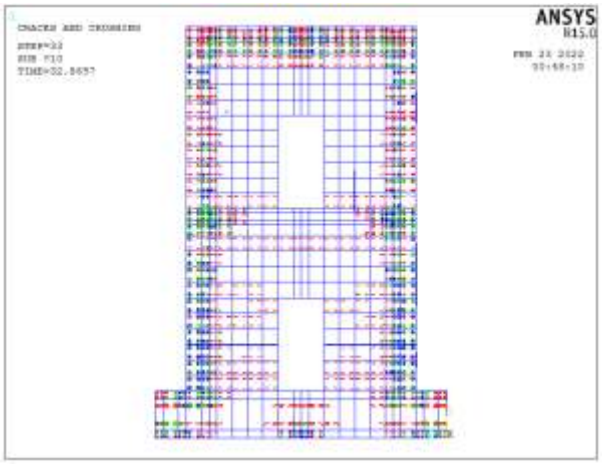

Fig. 27.E. Cracking pattern at cracking load (at ultimate load) for face with doors

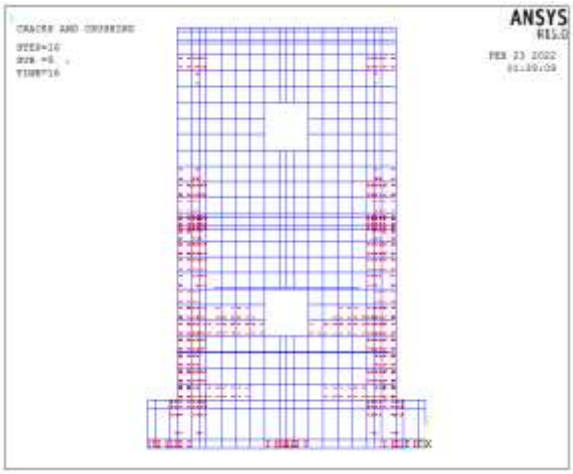

Fig. 27. C. Cracking pattern at cracking load (at frisk crack) for face with windows

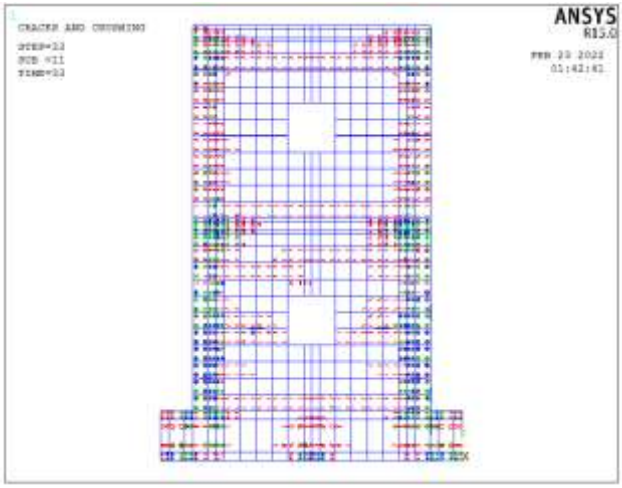

Fig. 27.F. Cracking pattern at cracking load (at ultimate load) for face with windows

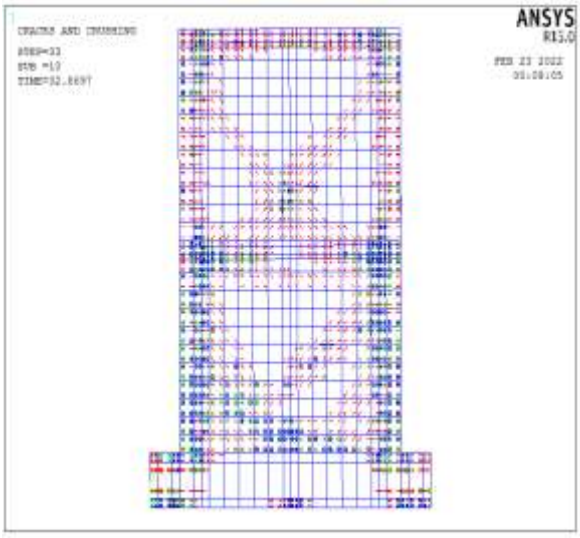

Fig. 27. D. Cracking pattern at cracking load (at ultimate load) for solid face.

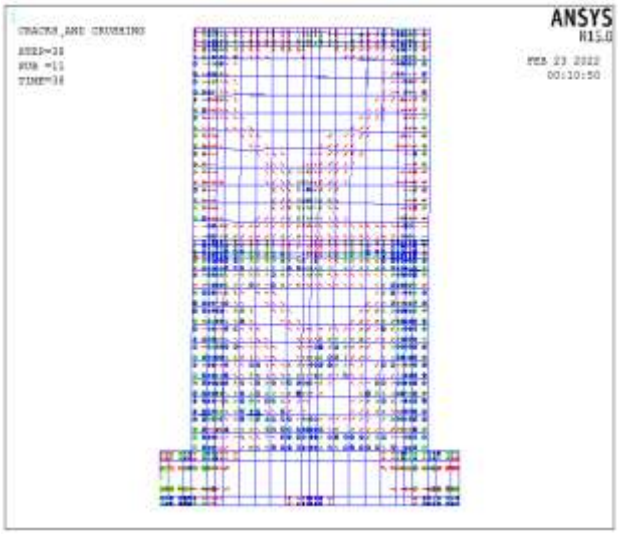

Fig. 27.G. Cracking pattern at cracking load (at failure load) for solid face

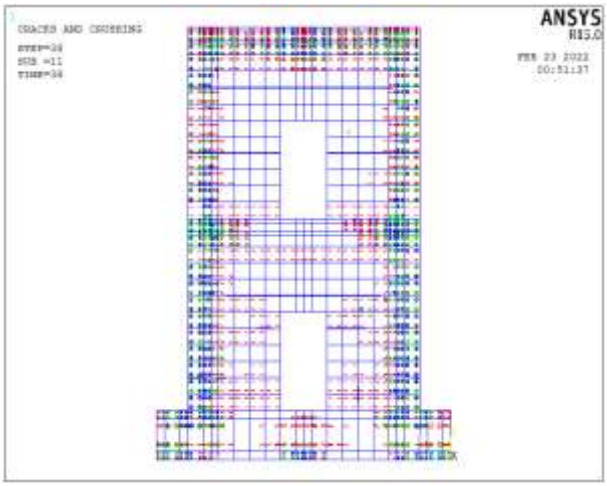

Fig. 27.H. Cracking pattern at cracking load (at failure load) for face with doors

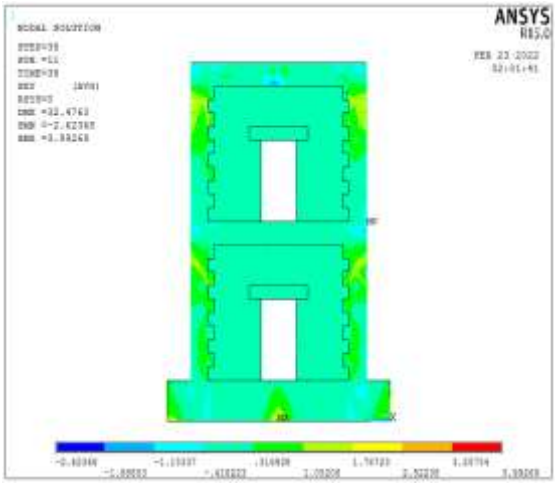

Fig. 27.K Shear stress (in Mpa) at ultimate load (face with doors).

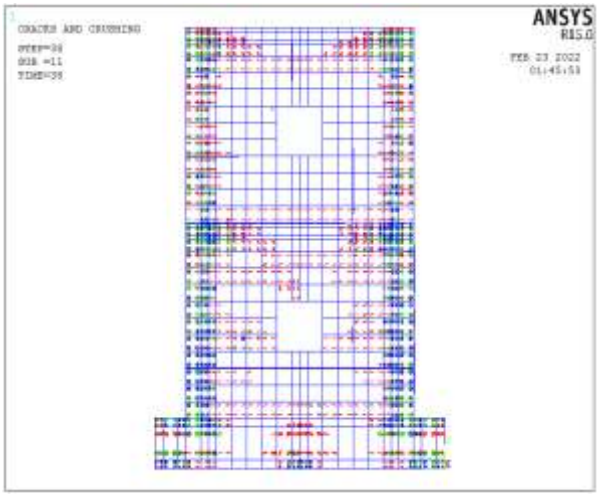

Fig. 27.I**.** Cracking pattern at cracking load (at failure load) for face with windows

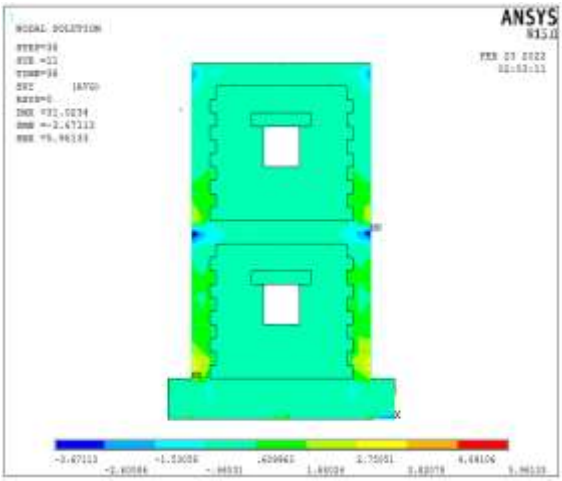

Fig 27.L**.** Shear stress (in Mpa) at ultimate load (face with windows).

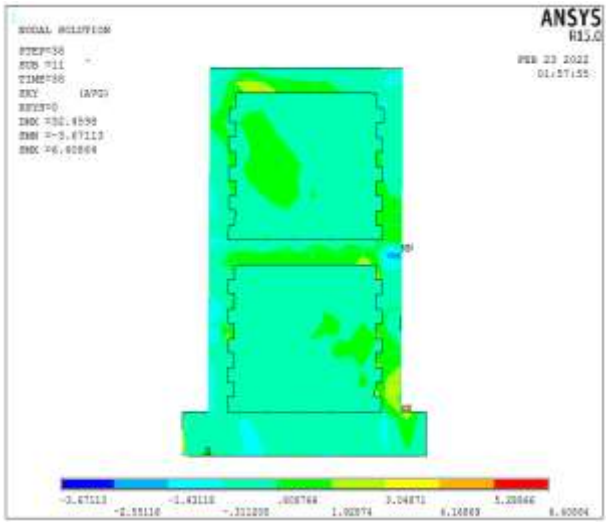

Fig. 27.J**.** Shear stress (in Mpa) at ultimate load (solid face).

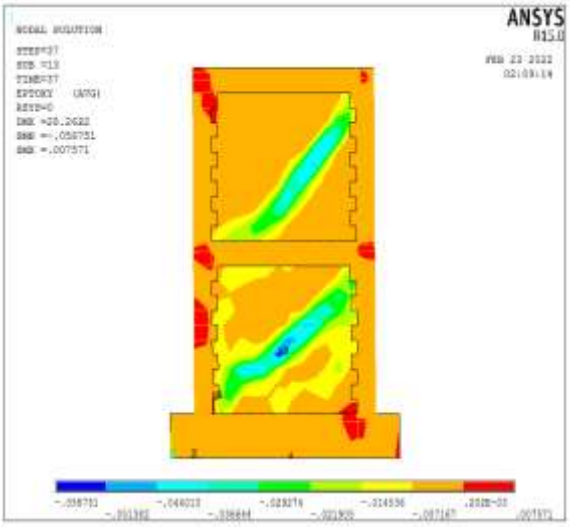

Fig .27.M. Mechanical strain at ultimate load (solid face) - at push case.

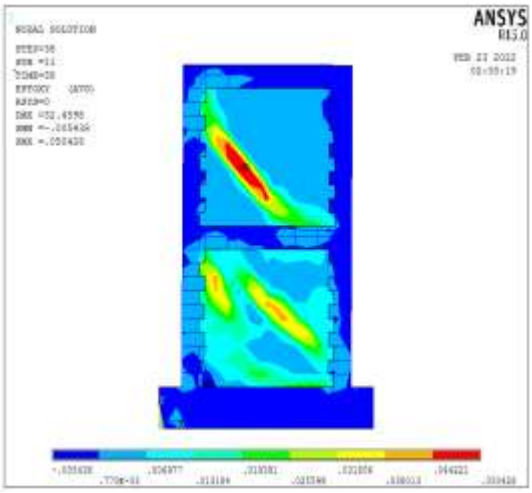

Fig .27.N**.** Mechanical strain at ultimate load (solid face) at pull case.

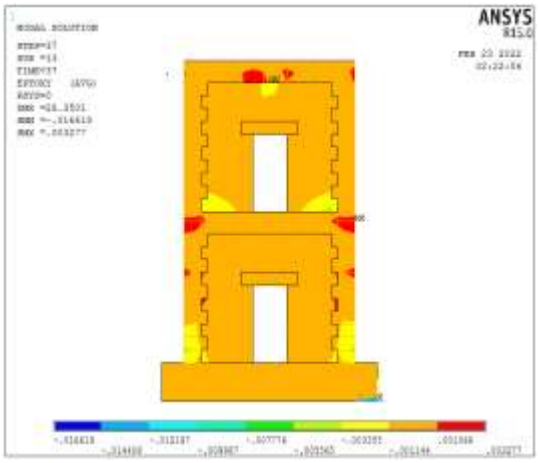

Fig .27.O**.** Mechanical strain at ultimate load (face with doors) at push case.

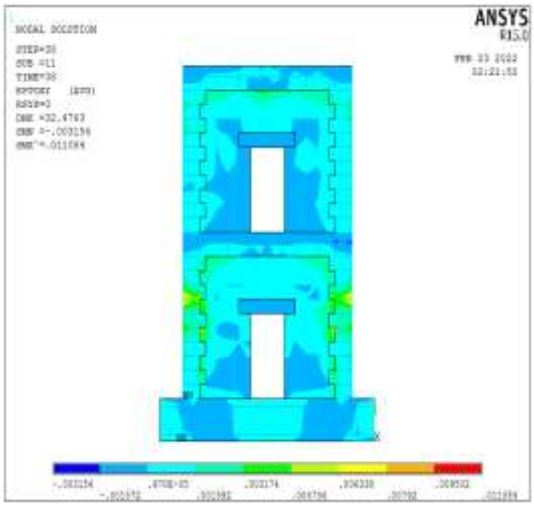

Fig. 27.P Mechanical strain at ultimate load (face with doors) at pull case.

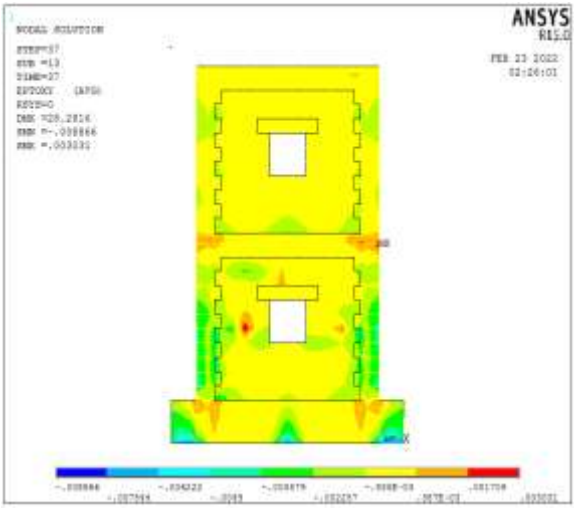

Fig. 27.Q**.** Mechanical strain at ultimate load (face with windows) at push case.

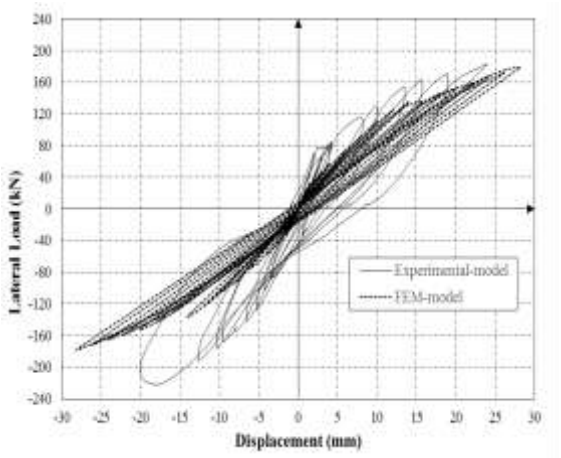

Fig.28.A**.** Hysteresis loops curves for experimental and finite model.

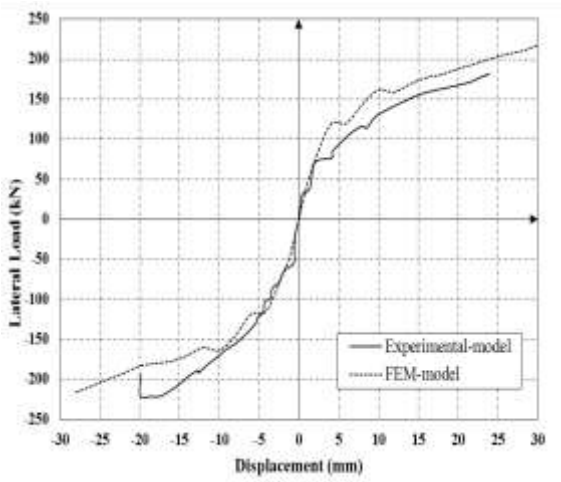

Fig. 28.B. Envelope load-displacement curves experimental and finite model.

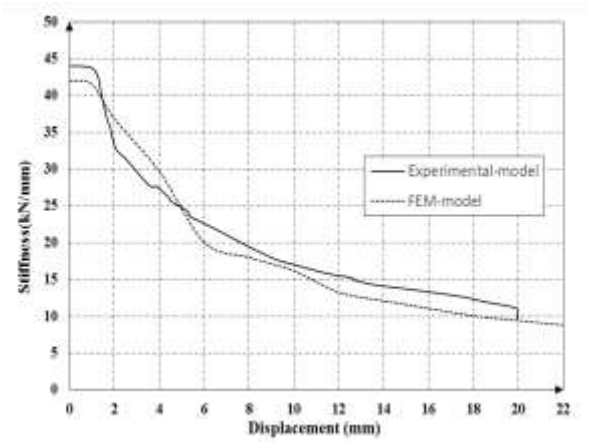

Fig. 28.C**.** Stiffness curves for experimental and finite model.

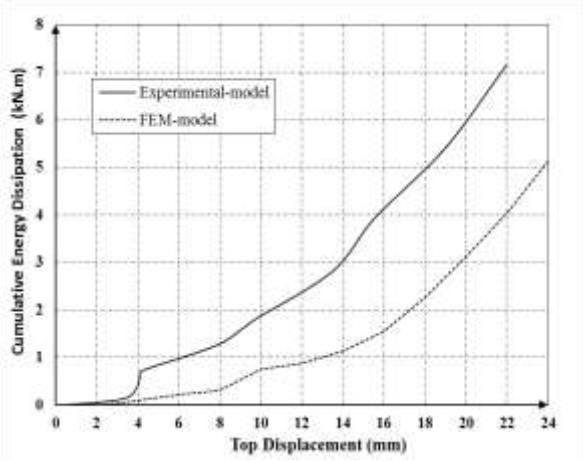

Fig. 28.D**.** Cumulative Energy Dissipation (KN.m) for experimental and finite model

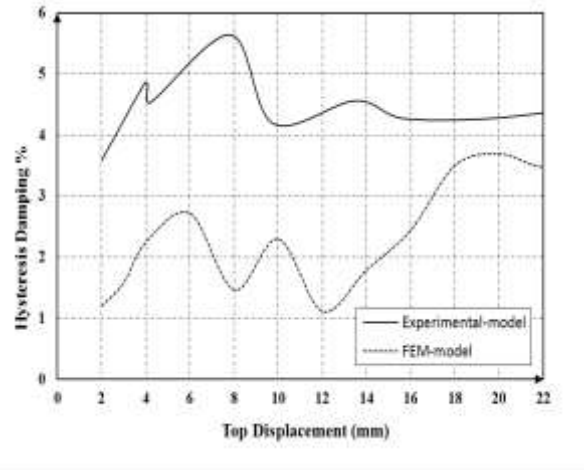

Fig.28.EHysteresis damping% for experimental and finite model

4. CONCLUSIONS

The structural behavior of a 3D restricted masonry building subjected to cyclic lateral load was investigated experimentally in this paper, and the results can be utilized to validate local standards to assure that the structure will perform satisfactorily under earthquake loads. Under quasi-static conditions, a half-scale two-story confined masonry building was tested. At the top of the building, lateral displacement controlled reverse cycle loads were applied to derive characteristics for force and displacement based seismic design. Crack pattern, lateral strength, drift, stiffness degradation, and energy dissipation capacity are some of the key elements of masonry construction systems investigated.

The following are some of the study's key findings:

1- With increasing lateral displacement, cracks appear in confined masonry specimen as: diagonal cracks at corners, marching towards tie-column and penetrating into tie-column; horizontal cracks at lower corners on out-of-plane walls, and crushing corner bricks of in-plane walls ends, causing longitudinal reinforcement to kink. Intersecting walls, slab, tie-beams and tie-columns connections were determined to be acceptable. However, the structural integrity of confined masonry buildings is greater between in-plane and out-plane walls, tie-columns, beams, and the slabs.

2- A diagonal shear crack propagated in confined elements can be classified as the specimen's failure mode.

3- The out- plane walls that are perpendicular to the direction of loading provided additional restraints for the in-plane wall movements, and enhanced overall the structural performance.

4- The structural response of a confined masonry infill walls were greatly enhanced in terms of strength and stiffness. More masonry walls will provide the structure more strength and ductility.

5- The developed model using finite element program ANSYS accurately simulates the behavior of experimental specimen and

accurately predicts the Crack pattern, lateral strength, drift, stiffness degradation, and energy dissipation capacity.

5. REFERENCE

[1] E Abdulahad and E Mahmud et al. 2018. "Seismic behaviour before and after strengthening of solid confined masonry walls with glass fiber reinforced polymers - analysis of hysteresis curves, obtained by shaking table tests"

[2] J. Martin Leal-Graciano, Basilia Quiñónez, Héctor E. Rodríguez-Lozoya, Juan J. Pérez-Gavilán, José F. Lizárraga-Pereda, Use of GFRP as retrofit alternative for confined masonry walls with window opening subjected to in-plane lateral load, Engineering Structures, Volume 223, 2020, 111148, ISSN 0141-0296,

[3] Ajay Chourasia, Shubham Singhal, Jalaj Parashar, Seismic performance evaluation of full-scale confined masonry building using light weight cellular panels, Journal of Building Engineering, Volume 32, 2020, 101473, ISSN 2352-7102,

[4] Mosaad El-Diasity, Hussein Okail, Osama Kamal, Mohamed Said, Structural performance of confined masonry walls retrofitted using ferrocement and GFRP under in-plane cyclic loading,Engineering Structures, Volume 94, 2015, Pages 54-69, ISSN 0141-0296,

[5] Jhair Yacila, Guido Camata, Jhoselyn Salsavilca, Nicola Tarque,Pushover analysis of confined masonry walls using a 3D macro-modellingapproach,EngineeringStructures, Volume 201,2019,109731,ISSN 0141-0296

[6] Perez G., et al, 2009. "Testing of masonry walls with different lengths: kinematics and lateral stiffness", XVII National Conference on Earthquake Engineering, Puebla, Mexico.

[7] Choayb, Belghiat & Jean-Patrick, P.L.A.S.S.I.A.R.D. & Messabhia, Ali & Ple, Olivier & Guenfoud, Mohamed. (2021). Analytical and numerical study of double-panel confined masonry walls. Journal of Building Engineering.39.102322.10.1016/j.jobe.2021.102322.

[8] Hatzinikolas, Michael & Korany, Yasser & Brzev, Svetlana. (2015). Masonry Design for Architects and Engineers. Canadian Masonry Publications ISBN: 978-0-9780061-1-2

[9] Roberto M., Brzev S., Maximiliano A., Teddy B., Francisco C., Junwu D., Mohammed F., Tim H., Ahmed M., Moghadam A., Daniel Q., Tomazevic M., Luis Y. (2011)."Seismic design guide for low-rise confined masonry buildings."

[10] Egyptian code of practice for design and construction of reinforced concrete structures (ECCS203-2018). Housing and Building Research Center, Giza, Egypt

[11] Tomazevic, M., and Klemence, I. (1997)."Verification of seismic resistance of confined masonry buildings."Earthquake engineering and structural dynamics, Vol. 26, 1073-1088

[12] Angelo M. and Enrique C. (2004) "Experimental Evaulation of Confined Masonry Walls with Several Confining-Columns" The 13th WCEE- World Conference on Earthquake Engineering, Canada, paper no. 2129.

[13] ANSYS® Academic Research, Release 15.0, ANSYS, Inc

[14] Hemant B. Kaushik1; Durgesh C. Rai2; and Sudhir K. Jain, (2007), "Stress-Strain Characteristics of Clay Brick Masonry under Uniaxial Compression", Journal of Materials in Civil Engineering, Vol. 19, No. 9, ASCE, pp. 728-739.

[15] [15]Ana Issa Cruz O., J.J. Perez Gavilan, Seismic performance of confined masonry walls with joint reinforcement and aspect ratio: An experimental study, Engineering Structures, Volume 242, 2021, 112484, ISSN 0141-0296

[16] Chaogang Qin, Guoliang Bai, Tao Wu, Bo Wang, Guangming Fu, Seismic behavior of unreinforced and confined masonry walls using innovative sintered insulation shale blocks under cyclic in-plane loading, Construction and Building Materials, Volume 268, 2021, 121063, ISSN 0950-0618.,

[17] Nasiri, Ehsan & Liu, Yi. (2019). The out-of-plane behaviour of concrete masonry infills bounded by reinforced concrete frames. Engineering Structures. 184. 406-420. 10.1016/j.engstruct.2019.01.098.

[18] A A Gumilang S and M Rusli,Seismic performance of earthquake resistant simple residential confined masonry house structure based on permen PUPR No.5 of 2016 specification.,2nd International Conference on Disaster and Management,IOP Conf. Series: Earth and Environmental Science 708 (2021) 012085,doi:10.1088/1755-1315/708/1/012085

[19] Safarizki, Hendramawat & Marwahyudi, Marwahyudi. (2021). Determining initial damage state of confined masonry wall. Journal of Physics: Conference Series. 1912. 012058. 10.1088/1742-6596/1912/1/012058.

[20] Borah, Bonisha & Kaushik, Hemant & Singhal, Vaibhav. (2020). Finite Element Modelling of Confined Masonry Wall under In-plane Cyclic Load. 10.1088/1757-899X/936/1/012020.